JOURNAL OF COLLOID AND INTERFACE SCIENCE 158, 317–325 (1993)

Quantifying Double-Layer Repulsion between a Colloidal Sphere and a Glass Plate Using Total Internal Reflection Microscopy

SCOTT G. FLICKER, JENNIFER L. TIPA, AND STACY G. BIKE[1]

Department of Chemical Engineering, The University of Michigan, Ann Arbor, Michigan 48109-2136

Received September 28, 1992; accepted January 28, 1993

Total internal reflection microscopy (TIRM) has recently been developed as a technique to measure the mean potential energy of interaction between a single colloidal particle and a flat plate. Based on the total internal reflection of light at an interface separating two media of different refractive indices, TIRM provides an instantaneous measurement of the separation distance between the particle and the plate. The distance measurements are derived from measurements of scattering intensity as the particle interacts with the evanescent wave formed upon total internal reflection. We have used TIRM to quantify double-layer repulsion acting between a glass plate and polystyrene latex spheres of diameters 7, 10, and 15 μm dispersed in aqueous solutions of ionic strengths from 0.2 to 3.0 mM. This work extends our earlier measurements of double-layer potential energies in that we are now able to measure the absolute separation distance between the sphere and the plate. The potential energy profiles agree very well with those predicted by a model of double-layer and gravity forces that involves no adjustable parameters. The measured double-layer potential energy is accurately described by a simple exponential model based on the linear superposition of potential profiles and Derjaguin's approximation, with the Debye length as the decay length.

INTRODUCTION

It is inherently difficult to measure the forces acting between colloidal particles *in situ*, primarily due to the submicrometer size of the particles and the small magnitude of the forces. As a result, techniques to measure such forces directly have employed macroscopic surfaces held at nanometer separations (1–3). In the well-known surface forces apparatus (3), for example, molecularly smooth sheets of mica are glued onto the crossed quartz cylinders with a radius of curvature on the order of 1 cm. The cylinders are pushed together with a known force, and the resulting equilibrium separation distance between the cylinders is measured to within 1 Å by multiple-beam interferometry. This apparatus has successfully measured a variety of forces including van der Waals and double-layer forces (3, 4), solvation forces (5), steric repulsion (6), and adhesion forces (7). Note, however, that the radius of curvature of the cylinders is at least four orders of magnitude larger than that of the typical colloidal particle. As a result, the surface forces apparatus cannot mimic the dynamic behavior of colloidal particles.

Consider a colloidal particle located near a flat surface. At equilibrium, the separation distance between the particle and the surface will fluctuate due to the Brownian motion of the particle. Assuming that the distribution of separation distances is described by a Boltzmann distribution, profiles of the mean potential energy can then be derived from the distance distributions.[2] Based on this principle, Prieve and Alexander developed a hydrodynamic technique to measure the instantaneous separation distance between a single colloidal sphere and a flat plate (8, 9). Using the hydrodynamic analysis of Goldman *et al.* (10), separation distances were inferred from measurements of the translational speed of the particle during slow linear shear flow of glycerol/water solutions. The resulting potential energy profiles demonstrated the presence of double-layer repulsion. In the range of submicrometer separation distances probed, however, the particle speed is not very sensitive to changes in the separation distance; as a result, this hydrodynamic technique has a spatial resolution on the order of 10 nm.

A new technique—total internal reflection microscopy (TIRM)—has recently been developed that also builds on the idea of monitoring the Brownian fluctuations of a colloidal particle located near a surface (11–17). Similar to the hydrodynamic technique, TIRM provides a measurement of the instantaneous separation distance, yet has a spatial resolution on the order of 1 nm. The separation distance is inferred from the intensity of light scattered by the particle as it interacts with an evanescent wave formed upon total internal reflection of light at an interface separating two media of different refractive indices. The scattered light intensity provides an exponentially sensitive measure of the instantaneous distance at which the particle is located from the interface.

[1] To whom correspondence should be addressed.

[2] In contrast, the surface-forces apparatus provides a direct measurement of the mean force.

0021-9797/93 $5.00

TIRM has been successfully used to measure gravity and weak double-layer forces acting on a micrometer-size polystyrene latex sphere located near a flat glass plate (11–13) in addition to measuring hindered diffusion coefficients of a colloidal sphere located near a flat plate (13, 14). Brown *et al.* (15, 16) coupled TIRM with radiation pressure to provide the first measurements of the absolute separation distance between the colloidal sphere and the plate. Of note is that solvent exchange is possible when the sphere is held in a fixed position by radiation pressure, which permits one to study the same particle under a variety of conditions. Brown *et al.* did observe an unexplained deviation from the expected exponential decay of the scattering intensity at small separation distances, however. More recently, Walz and Prieve (17) have verified that the exponential decay is valid down to contact for spheres less than approximately 30 μm in diameter.

Of note is that atomic force microscopy (AFM) has recently been used to measure surface forces between a colloidal sphere and a flat silica surface in aqueous solutions (18). The colloidal particle is glued to the cantilever tip of the instrument, and the deflection in the tip is measured as the particle is brought in the vicinity of the substrate. Unlike TIRM, however, Brownian motion of the particle is not allowed by virtue of being fixed on the cantilever tip.

In this paper, we describe the use of TIRM to quantify the electrostatic double-layer forces between a glass microscope slide and polystyrene latex spheres of nominal diameters 7, 10, and 15 μm dispersed in aqueous solutions of low ionic strengths (0.2 to 3.0 mM). Note that by working at low ionic strengths, we are able to neglect the contribution from van der Waals attraction of the particle's movement. This work extends our earlier efforts (19) in that we are now able to measure absolute separation distances between the particle and the glass slide, using the results of Walz and Prieve. Distributions of separation distance between a single sphere and the glass slide are calculated from the scattering intensity measurements. The most-probable separation distances are found to vary from 59 to 175 nm. Potential energy profiles constructed from the histograms not only demonstrate the influence of both double-layer repulsion and gravity on the sphere's movement, but they also agree very well with potential energies predicted from models of these forces. The double-layer potential energy as a function of separation distance is calculated by subtracting the known gravitational potential energy from the total potential energy of interaction. This double-layer potential energy is accurately described by a simple exponential model based on the linear superposition of potential profiles and Derjaguin's approximation, with the Debye length as the decay length.

This work illustrates the potential of TIRM to quantify colloidal forces in a variety of systems. In particular, we are presently extending the TIRM technique to quantify nonspecific interactions in biological systems, thus providing fundamental insight into the process of cell–substrate adhesion and the mechanistics of nonspecific forces including steric, undulation, and hydration forces. In addition, our work suggests the application of TIRM to study polymer-induced flocculation of colloidal particles.

BACKGROUND

Total Internal Reflection Microscopy

TIRM is based on the total internal reflection of light at an interface separating two transparent media of different refractive indices. When a beam of light is incident on such an interface, the light is partially reflected back into the first medium ("1") and partially transmitted into the second medium ("2") (Fig. 1). The angle of refraction ϕ of the transmitted beam is given by Snell's law (20)

$$\sin \phi = (n_{21})^{-1} \sin \theta. \qquad [1]$$

θ is the angle of incidence and $n_{21} \equiv n_2/n_1$, where n_i is the refractive index of medium i. When the light is internally reflected (i.e., $n_1 > n_2$), θ is always less than ϕ. When ϕ is equal to 90° the corresponding incident angle is designated as the critical angle $\theta_c = \sin^{-1} n_{21}$. For $\theta > \theta_c$, ϕ is imaginary and the light is totally reflected at the interface.

While no visible light propagates into the less-optically-dense medium upon total internal reflection, an evanescent electromagnetic wave does penetrate a short distance into this medium. The intensity I_{ev} of this evanescent wave decays exponentially with the distance z from the interface (20)

$$I_{ev}(z) = I_{ev}(0) \exp\left(-\frac{z}{d_p}\right), \qquad [2]$$

where $I_{ev}(0)$ is the intensity of the evanescent wave at the interface. d_p is the characteristic penetration depth of the evanescent wave, the distance at which I has decayed to $1/e$ of $I_{ev}(0)$

$$d_p = \frac{\lambda_0/n_1}{4\pi(\sin^2\theta - n_{21}^2)^{1/2}}, \qquad [3]$$

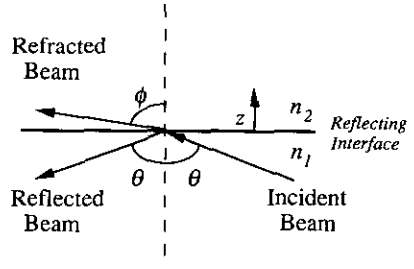

FIG. 1. Illustration of internal reflection at an interface separating two media of different refractive indices ($n_1 > n_2$). θ is the angle of incidence and ϕ is the angle of refraction.

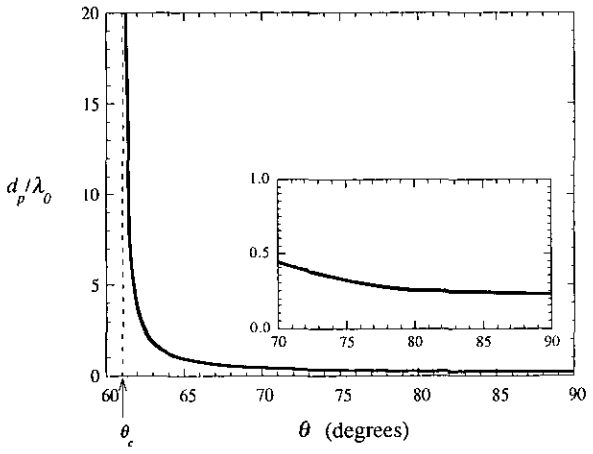

FIG. 2. Dependence of the decay length on incident angle for total internal reflection at a glass/water interface.

where λ_0 is the wavelength of light in a vacuum. As illustrated in Fig. 2, for given media 1 and 2 and wavelength λ_0, d_p can be altered simply by changing the angle of incidence θ. In particular, d_p approaches infinity as θ approaches θ_c, while d_p is a few tenths of the wavelength of light for θ close to 90° ("glancing" incident angle).

Any material of refractive index $n_3 \neq n_2$ that interacts with the evanescent wave will absorb energy from this electromagnetic wave and subsequently scatter light. This phenomenon has formed the basis of the total internal reflection fluorescence (TIRF) technique (21), in which fluorescently tagged molecules located in the evanescent wave absorb radiation at the wavelength of the incident light and then fluoresce at a different wavelength. TIRM, on the other hand, does not rely on the presence of fluorescing species that interact with the evanescent wave. Instead, an object of unmatched refractive index located in the evanescent wave scatters radiation at the same wavelength as the incident light. Chew *et al.* (22) have shown that dielectric spheres located in an evanescent wave scatter radiation at an intensity that decays exponentially with the separation distance h between the sphere and the reflecting interface

$$I_{sc}(h, \Omega) = I_{sc}(0, \Omega)\exp\left(-\frac{h}{d_p}\right), \qquad [4]$$

where $I_{sc}(0, \Omega)$ is the scattered light intensity for a sphere in contact with the reflecting interface ($h = 0$) and Ω is a fixed angle over which the scattered light is collected. Note that for the remainder of this paper, we will refer to the scattered light intensity simply as "I."

While Eq. [4] is derived for particles located far enough away from the reflecting interface so that multiple reflections can be neglected, Walz and Prieve have shown that this exponential decay is valid for any separation distance for spherical particles less than approximately 30 μm in diameter (17). Consequently, we have used Eq. [4] to transform the measured scattering intensities into separation distances for spheres of diameters from 7 to 15 μm. The scattering intensity at $h = 0$ is determined simply by adsorbing the particle to the reflecting interface through the addition of excess electrolyte. Then, the scattered light intensity provides an exponentially sensitive measure of the separation distance between the sphere and the interface.

Model for the Total Potential Energy

Consider a sphere dispersed in an electrolyte solution and located near a flat plate. The total potential energy $V(h)$ can be written as

$$V(h) = V_A(h) + V_R(h) + V_g(h), \qquad [5]$$

where $V_A(h)$, $V_R(h)$, and $V_g(h)$ are the van der Waals, double-layer, and gravitational potential energies, respectively. For the experimental systems that we have studied, the contribution from van der Waals attraction to the total potential is negligible (9). Thus, it is necessary to consider only the contributions from double-layer and gravity forces to the total potential energy.

For thin, slightly overlapping counterion clouds, the double-layer potential energy between a spherical particle and a flat plate is given by (23)

$$V_R(h) = 16\epsilon a\left(\frac{kT}{ze}\right)^2 \tanh\left(\frac{ze\psi_s}{4kT}\right)\tanh\left(\frac{ze\psi_p}{4kT}\right)\exp(-\kappa h), \qquad [6]$$

where ϵ is the dielectric constant of the fluid, a is the radius of the sphere, kT is the thermal energy, z is the ion valency (assuming a symmetric electrolyte), e is the protonic charge, κ is the inverse Debye length, and ψ_s and ψ_p are the surface potentials of the sphere and the plate, respectively. This model for the double-layer potential energy, which is based on the linear superposition of the potential profiles on opposing surfaces and Derjaguin's approximation, is valid for *all* values of surface potentials provided that $\kappa a \gg \kappa h \gg 1$. Note that this model predicts a simple exponential dependence on the separation distance h.

The gravitational potential energy is given by

$$V_g(h) = \frac{4}{3}\pi a^3 \Delta\rho g h. \qquad [7]$$

$\Delta\rho$ is the difference between the particle and the fluid densities and g is the gravitational acceleration. Since the particle sizes used in this work are accurately known, we can subtract the gravitational contribution as given by Eq. [7] from the measured total potential energy to yield the double-layer po-

tential energy. This has allowed us to compare the measured double-layer potential energy with that predicted by Eq. [6] to validate the applicability of linear superposition and Derjaguin's approximation for our experimental systems.

Using Eqs. [6] and [7], the total potential energy can then be simply written as

$$V(h) = B\exp(-\kappa h) + Gh, \qquad [8]$$

where the parameters B and G depend only on material properties and temperature:

$$B = 16\epsilon a\left(\frac{kT}{ze}\right)^2 \tanh\left(\frac{ze\psi_s}{4kT}\right)\tanh\left(\frac{ze\psi_p}{4kT}\right) \qquad [9]$$

$$G = \frac{4}{3}\pi a^3 \Delta\rho g. \qquad [10]$$

At equilibrium, the sphere will locate at the position h_m where the total potential energy is a minimum. From Eq. [8], this separation distance is given by

$$h_m = \kappa^{-1}\ln\left(\frac{B\kappa}{G}\right). \qquad [11]$$

EXPERIMENTAL

Apparatus

Shown in Fig. 3a is a sketch of the TIRM apparatus which incorporates a Nikon Microphot microscope located on a Newport vibration-isolation table. The light source used to generate the evanescent wave is a multiline 100-mW Ar ion laser (Ion Laser Technology) operating at a wavelength of 514.5 nm and a power of 5 mW. The light from the laser is directed to a dove prism using two first-surface aluminum mirrors mounted on a beam-steering apparatus. The upper mirror is attached to a rotating stage, which permits control of the incident angle θ. The prism is mounted on a modified microscope stage that can translate in three directions.

As detailed in Fig. 3b, a glass microscope slide is optically coupled to the prism using index-matched immersion oil. Total internal reflection of the laser beam then occurs at the upper surface of the glass slide. A dilute dispersion is placed in a glass well fused to the microscope slide. Using the translating stages, the slide is moved to focus on one particle interacting with the glass slide. The light scattered by the selected particle is captured by a 40× water-immersible objective (Zeiss) and subsequently filtered using an Omega bandpass filter (514.5 nm). The intensity of the scattered light is then monitored by a Hamamatsu R1104 photomultiplier tube (PMT) driven by a Bertan Model 215 high voltage power supply and incorporating a user-made dark current suppression circuit. The PMT generates a current that is linearly proportional to the intensity; this current is amplified and converted to a voltage using a Keithley Model 470 current amplifier. The resulting analog signal is sampled at a known rate by a Keithley Model 500 data acquisition system, and the discrete output is stored on an IBM PS/2 Model 70 for later analysis.

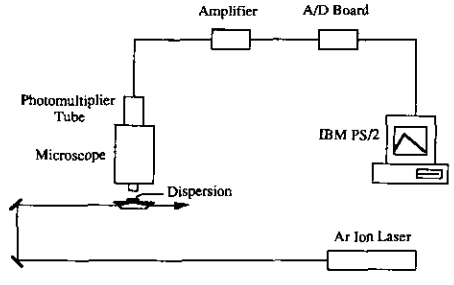

FIG. 3a. Sketch of TIRM apparatus.

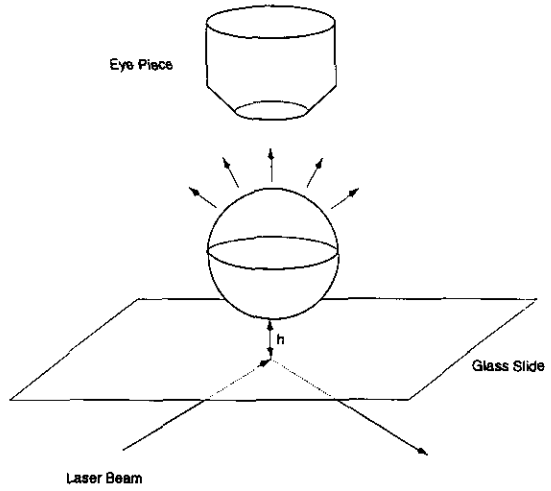

FIG. 3b. Magnified view of scattering assembly.

Materials

The colloidal particles studied were polystyrene latex spheres of diameters 7.04 ± 0.04, 9.87 ± 0.06, and 15.00 ± 0.09 μm from Duke Scientific. Hereafter, we will refer to these particle sizes by their nominal diameters of 7, 10, and 15 μm, respectively. The particles were dispersed in aqueous solutions prepared by adding a known amount of a filtered 0.1 M NaCl (Fisher Scientific ACS grade) stock solution to filtered deionized water containing 0.05 mM of the nonionic surfactant octaethyleneglycol mono-n-decyl ether (Nikko Chemical Co. Ltd.). The ionic strength of each dispersion was calculated from pH and conductivity measurements. Four ionic strengths were used in this work: 0.20, 0.50, 1.0, and 3.0 mM. These low ionic strengths enabled us to neglect van der Waals attraction and employ the potential energy model described in the previous section. The corresponding Debye lengths calculated from the conduc-

tivity and pH measurements are, in order of increasing ionic strength, 21.5, 13.6, 9.61, and 5.55 nm.

Methods

Prior to each experiment, the laser was warmed up at full power for 30 min to ensure stable operation. After this warm-up period, the laser power was reduced to 5 mW. Approximately 0.5 ml of a selected dispersion was placed in the glass well on the microscope slide. The objective was carefully lowered into the dispersion, and the exposed liquid surface was covered with Parafilm to prevent evaporation and a corresponding change in ionic strength.

After focusing on particles near the bottom of the glass well, a single particle that was separated by at least 7 particle diameters from other particles was centered in the field of view of the microscope. A rectangular slit aperture in the microscope was then adjusted to allow the PMT to "see" an area of approximately 3 particle diameters square. This area was sufficient to allow the particle to diffuse parallel to the glass slide surface during an experiment without leaving the aperture window. The point of reflection of the laser beam was then positioned directly under the particle, as determined by maximizing the detected scattered light intensity.

Each experiment consisted of recording at least 20,000 measurements of the scattering intensity at a sampling rate of 5 ms. Before each experiment, the particle was moved just outside of the field of view, and the background intensity recorded. This background intensity was later subtracted from the measured scattering intensity to give a true value of the scattering intensity.

Data Analysis

Histograms. The histograms of frequency, $N[I(h)]$, as a function of the scattering intensity, $I(h, \Omega)$, are constructed in the following manner. The mean background intensity is subtracted from each measurement of the scattering intensity to yield the true scattering intensity, assuming that the angle Ω is constant. The time series data for each experiment are then converted into a histogram, which is condensed by combining frequencies in the range $I - \Delta I$ to $I + \Delta I$ into one interval. Typically, ΔI ranged from 50 to 200 (in arbitrary units) while I ranged from 0 to 8000.

The maximum in the histogram corresponds to the location designated h_2, which may not be equivalent to the most-probable separation distance based on a balance of forces, designated h_m (11). Instead, the shape of the histogram represents the shape of the probability density function for intensity, $P(I)$, while $p(h)$ is the probability density function for the separation distance. Consequently, the separation distance h_2 at which $dP/dI = 0$ is not necessarily equal to the separation distance h_m at which $dp/dh = 0$. We denote the maximum frequency and the corresponding intensity as $N[I(h_2)]$ and $I(h_2)$, respectively.

Potential energy profiles. The scattering histograms are then converted into potential energy profiles ($V(h)$ as a function of h) as summarized below (11). Rewriting Eq. [4], the separation distance h is related to the measured scattered light intensity at that distance by

$$h = d_p \ln\left(\frac{I(0)}{I(h)}\right). \qquad [12]$$

Assuming that the probability of finding a particle at one location relative to another is represented by a Boltzmann distribution, the potential energy $V(h)$ relative to that at h_2, $V(h_2)$, is given by

$$\frac{V(h) - V(h_2)}{kT} = \ln\left(\frac{N[I(h_2)]I(h_2)}{N[I(h)]I(h)}\right). \qquad [13]$$

The potential is made dimensionless by dividing by kT.

We compare our experimental potential energy profiles with those predicted from the model described in the previous section. Combining Eqs. [8] and [11], the total potential relative to that at h_m is

$$\frac{V(h) - V(h_m)}{kT} = \frac{G}{kT}\left(\frac{\exp[-\kappa(h - h_m)] - 1}{\kappa} + (h - h_m)\right). \qquad [14]$$

Note that Eq. [14] has no adjustable parameters: the inverse Debye length κ is calculated from the measured solution conductivity and pH. In addition, the parameter B is not needed to evaluate Eq. [14]; this is fortuitous since the parameter B includes the surface potentials of the sphere and the glass slide, which are difficult to evaluate *in situ*.

RESULTS AND DISCUSSION

Histograms of scattering intensity for four 15-μm spheres each in a solution of different ionic strength are shown in Fig. 4. Similar histograms were obtained for the 5- and 10-μm particles. Note that the peak maxima, designated by $[I(h_2), N(h_2)]$, are displaced to higher relative intensities as the ionic strength is increased. The decrease in the Debye length with increasing ionic strength leads to a weakening in double-layer repulsion and correspondingly a decrease in the most-probable separation distance. This decrease in separation distance, in turn, leads to an increase in scattering intensity (Eq. [4]). The peak widths also increase with increasing ionic strength. This peak broadening is caused by the exponential dependence of the scattered light intensity on the separation distance.

Note also that the histograms are not symmetric about the intensities corresponding to the maximum frequencies.

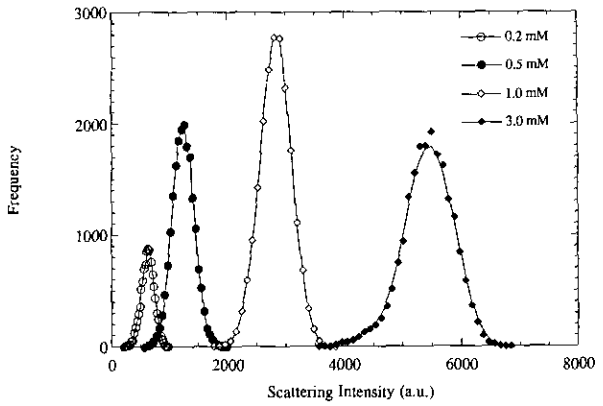

FIG. 4. Histograms of scattering intensity for four 15.00-μm polystyrene latex spheres each dispersed in a solution of different ionic strength from 0.20 to 3.0 mM.

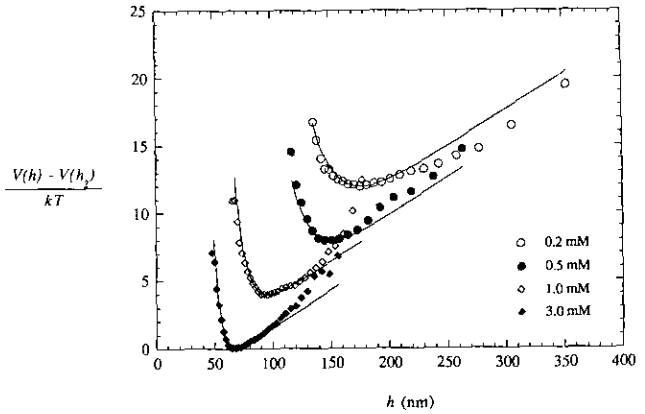

FIG. 6. Potential energy profiles for four 9.87-μm polystyrene latex spheres each dispersed in a solution of different ionic strength from 0.20 to 3.0 mM. The potential energy curves have been shifted vertically by 4 dimensionless energy units for ease of viewing. The symbols are the experimental data and the solid lines are the model predictions.

For scattering intensities less than $I(h_2)$, the slower decrease in frequency with decreasing intensity reflects the influence of the gravitational potential which varies with the first power of the separation distance. Electrostatic repulsion dominates at smaller separation distances, or equivalently higher scattering intensities. The expected exponential variation of the double-layer potential with separation distance gives rise to a faster decrease in frequency with increasing scattering intensity for intensities greater than $I(h_2)$.

Shown in Figs. 5–7 are the potential energy profiles derived from the scattering histograms. The dimensionless relative potential energy $[V(h) - V(h_2)]/kT$ is plotted versus the absolute separation distance h between the particle and the glass slide. The symbols correspond to the experimental data while the solid lines are predicted from the model given by Eq. [14], using the calculated Debye lengths based on solution conductivity and pH measurements. Note that the minimum of each potential profile should lie on the x-axis, corresponding to a zero relative potential; for ease of viewing, adjacent potential energy curves in the same figure are shifted vertically by 4 kT units.

The potential energy profiles for the 15-μm particles are shown in Fig. 5. Each potential energy profile corresponds to a single (but different) particle. The experimental data and the model predictions agree very well, especially for separation distances less than h_2 (corresponding to the minimum in the potential profile). In this region, the potential energy profiles display an increasing slope with increasing ionic strength, reflecting the decrease in double-layer repulsion. Note also that a small deviation of the experimental data

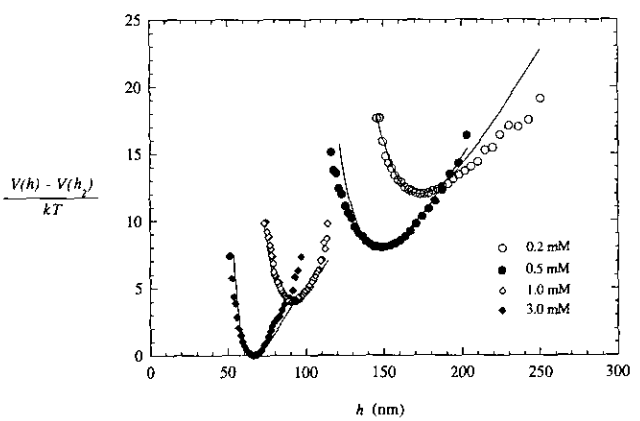

FIG. 5. Potential energy profiles for four 15.00-μm polystyrene latex spheres each dispersed in a solution of different ionic strength from 0.20 to 3.0 mM. The potential energy curves have been shifted vertically by 4 dimensionless energy units for ease of viewing. The symbols are the experimental data and the solid lines are the model predictions.

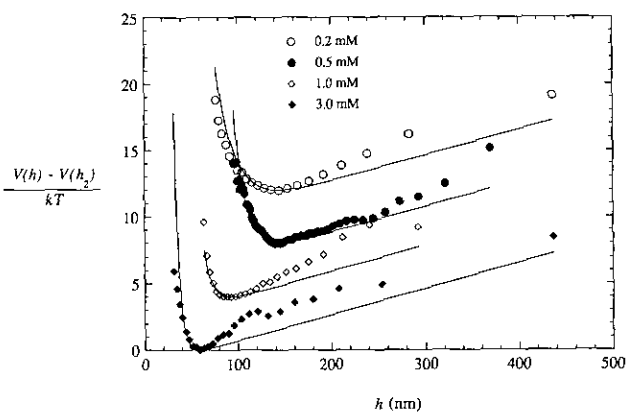

FIG. 7. Potential energy profiles for four 7.04-μm polystyrene latex spheres each dispersed in a solution of different ionic strength from 0.20 to 3.0 mM. The potential energy curves have been shifted vertically by 4 dimensionless energy units for ease of viewing. The symbols are the experimental data and the solid lines are the model predictions.

from the model prediction is seen in this region for the 0.5 mM solution; this deviation will be discussed later. For separation distances much greater than h_2, the double-layer force is negligible; then, the slopes of the potential energy profiles become constant and equal to the net weight of the particle.

The separation distance h_2 corresponding to the potential minimum decreases as the ionic strength increases. In addition, the range of separation distances that the particle samples decreases as the ionic strength increases. These trends reflect the screening of double-layer repulsion with increasing ionic strength. Note also that the spatial resolution in the separation distance is on the order of a nanometer; of course, this resolution is dependent on the condensing interval ΔI selected for the scattering intensity histogram.

Figure 6 shows the corresponding potential energy profiles for the 10-μm particles. Similar to the 15-μm particles, the most probable separation distance decreases as the ionic strength increases. In addition, the range of separation distances sampled by the particle decreases as the ionic strength increases. For the given ionic strengths, the particle samples distances from 50 to 350 nm above the glass slide.

Good agreement is seen between the experimental data and the model predictions for separation distances less than h_2, for which double-layer repulsion is dominant. For $h > h_2$, the slope of the potential energy profiles is less than that for the 15-μm particles, due to the smaller net weight of the 10-μm particles. Deviations between the measured and expected potential energies are noted in this region, however. That the experimental potential energy values are greater than those predicted for the 0.5, 1.0, and 3.0 mM solutions suggests that the particle is experiencing an additional attractive force that restricts its motion. Such a force might result from the presence of a "tether," or extended polymer chain, on the particle that is attached to the glass slide (24); this observation suggests the application of TIRM to study polymer-induced flocculation of colloidal particles. An alternate explanation is that the particle is located directly above an asperity on the glass slide that restricts the motion of the particle. The first explanation seems more likely, however, since the expected potential energy profiles deviate from the model only at large separation distances.

The potential energy curves for the 7-μm particles are shown in Fig. 7. The agreement between the experimental data and the model predictions is good for separation distances less than h_2. The model is thus able to predict the influence of double-layer repulsion on the movement of the particle.

Systematic positive deviations are noted for $h > h_2$, however, as were also noted in our earlier work (19). While these positive deviations imply that the particles do not sample separation distances greater than h_2 as frequently as expected, we instead attribute the deviations to a loss of resolution resulting from the smaller size of the 7-μm particles as compared to the larger 10- and 15-μm particles. At a given separation distance, the 7-μm particles generate a smaller scattering intensity than that generated by either the 10- or 15-μm particles. Moreover, because of their smaller net weight, the 7-μm-diameter particles diffuse to greater distances above the glass slide where the evanescent wave intensity and correspondingly the scattering intensity are significantly lower. For example, the separation distances sampled by the 7-μm particles range from 30 to 430 nm. Consequently, the particles diffuse to more than five times the penetration depth d_p away from the glass slide. At a separation distance of 430 nm, the scattering intensity is 1/130 of that when the separation distance and penetration depth are equal. The PMT is not only less sensitive to this lower scattering intensity but is also less able to resolve changes in the scattering intensity and thus the separation distance since the intensity of the evanescent wave changes very slowly with distance in this region far from the reflecting interface.

The measured equilibrium, or most probable, separation distances corresponding to the location of the potential minimum are given in Table 1. For a given particle size, the equilibrium separation distance decreases with increasing ionic strength. This trend is expected, as double-layer repulsion weakens with increasing ionic strength. The equilibrium separation distance is also expected to decrease as particle size increases for a given ionic strength, assuming that the particle surface potentials are functions of ionic strength only and are equal for particles of all sizes at a given ionic strength; this trend is not seen, however. In general, very little difference is noted among the separation distances for three particle sizes at the same ionic strength. This lack of a definite trend with particle size can be attributed to surface-potential variations. At this time, however, we are unable to verify that such variations are responsible for the noted deviations from expected behavior.

The double-layer potential energy can be calculated from the measured total potential energy by subtracting the known contribution from gravity. Shown in Fig. 8 is a plot of the dimensionless double-layer potential energy V_R/kT as a function of separation distance for the 15-μm particles. Note that the range of separation distances for which double-layer repulsion is dominant decreases as the ionic strength increases, demonstrating the weakening in double-layer re-

TABLE 1
Measured Equilibrium Separation Distances

Particle diameter (μm)	Measured equilibrium separation distance (nm)			
	0.2 mM	0.5 mM	1.0 mM	3.0 mM
7.04	144	145	92.6	59.1
9.87	175	151	95.8	68.0
15.00	174	149	90.0	66.2

pulsion at higher ionic strengths. Similar trends were also seen for the 7- and 10-μm particles. The data for each ionic strength can be described by a straight line, indicating that the simple exponential model of double-layer repulsion is applicable at these low ionic strengths.

In addition, the Debye length is found to be the correct decay length for the exponential model. Shown in Table 2 is a comparison between the Debye lengths (κ^{-1}) calculated from the measured solution conductivities and those calculated from the slopes of the double-layer potential energy as a function of separation distance. Good agreement is seen between the calculated Debye lengths and those measured from the experiments. Recall that for the 15-μm particle in the 0.5 mM solution the experimental potential energies deviated from the model predictions. Specifically, in the region $h < h_2$ the experimental potential energies are less than predicted, implying that the double-layer repulsive energy is greater than expected based on the Debye length calculated from the solution conductivity. This deviation is also seen in the comparison of the Debye lengths: the Debye length calculated from the slope of the double-layer potential energy as a function of distance is greater than that calculated from the measured solution conductivity.

The validity of the exponential model of double-layer repulsion can also be confirmed by calculating the surface potentials from the intercepts of the lines describing the double-layer potential energy as a function of separation distance (Fig. 8). The intercept corresponds to B/kT where the parameter B is given by Eq. [9]. When the dielectric constant of the medium, particle size, ion valency, and temperature are known, the surface potential of either the sphere (ψ_s) or the glass slide (ψ_p) can be calculated if the other potential is known. Scales *et al.* (25) have measured the zeta potential of fused silica slides as a function of both KCl concentration and pH. For low ionic strengths (0.1 to 1.0 mM) and at a pH typical of our deionized water, the zeta potential of the silica slide varies from −60 to −80 mV. Assuming an average

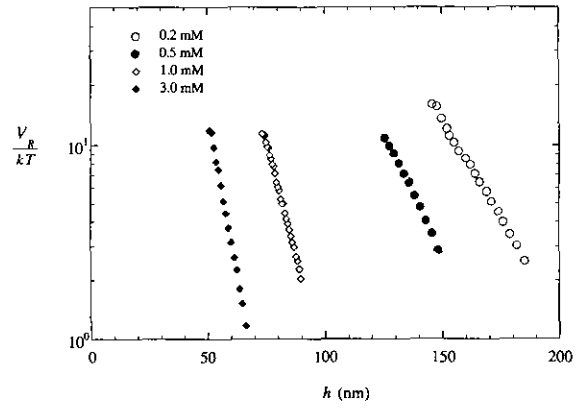

FIG. 8. Double-layer potential energy as a function of separation distance corresponding to the 15.00-μm particles in Fig. 5.

TABLE 2

Comparison of Debye Screening Lengths Calculated from Solution Conductivity and pH Measurements ("Predicted") and from Double-Layer Potential Energy Measurements

		κ^{-1} (nm) calculated from measured V_R		
I (mM)	Predicted κ^{-1} (nm)	7.04 μm diameter	9.87 μm diameter	15.00 μm diameter
0.20	21.5	24.0	23.0	21.5
0.50	13.6	15.2	14.0	17.4
1.0	9.61	8.41	9.34	9.47
3.0	5.55	7.03	5.92	6.64

value of −70 mV for our glass microscope slide in contact with low ionic strength NaCl solutions, we can then estimate the zeta potential of the polystyrene spheres studied (assuming that the surface potential is approximately equivalent to the zeta potential). For the four particles illustrated in Fig. 8, the zeta potentials are calculated to range from −15 to −30 mV; these values agree with previous zeta potential measurements in our laboratory. Thus, the simple model of double-layer repulsion based on linear superposition and Derjaguin's approximation is valid for our experimental systems.

SUMMARY

We have shown that TIRM can be used to measure double-layer forces between a single colloidal sphere and a flat plate. Potential energy profiles are derived for polystyrene microspheres of nominal diameters 7, 10, and 15 μm dispersed in aqueous solutions of ionic strengths from 0.2 to 3.0 mM. These profiles demonstrate the influence of gravity and double-layer repulsion on the movement of the spheres. In addition, the experimental potential energy profiles agree very well with those predicted from a model of gravity and double-layer forces that involves no adjustable parameters. The experimentally derived double-layer profiles confirm that a simple exponential model of double-layer repulsion based on linear superposition of potential profiles and Derjaguin's approximation describes the data well. The decay length of the double-layer profiles is found to be equivalent to the Debye length. Providing the capability to observe the dynamics of particle motion with the spatial resolution of scanning electron microscopy, TIRM has the potential to quantify colloidal forces in a variety of systems.

ACKNOWLEDGMENTS

We gratefully acknowledge the financial support of the National Science Foundation under Grants CTS-8907739 and CTS-9058078. S.G.F. thanks the Amoco Foundation for a graduate fellowship.

REFERENCES

1. Derjaguin, B. V., Titijevskaia, A. S., Abrikossova, I. I., and Malkina, A. D., *Discuss. Faraday Soc.* **18,** 24 (1954).
2. Tabor, D., and Winterton, R. H. S., *Proc. R. Soc. Ser. A* **312,** 435 (1969).
3. Israelachvili, J. N., and Adams, G. E., *J. Chem. Soc. Faraday Trans. 1,* **74,** 975 (1978).
4. Israelachvili, J. N., *Faraday Discuss. Chem. Soc.* **65,** 20 (1978).
5. Christenson, H. K., *J. Chem. Soc. Faraday Trans. 1* **80,** 1933 (1984).
6. Israelachvili, J. N., Tirrell, M., Klein, J., and Almog, Y., *Macromolecules* **17,** 204 (1984).
7. McGuiggan, P. M., and Israelachvili, J. N., *J. Mater. Res.* **5,** 2232 (1990).
8. Prieve, D. C., and Alexander, B. M., *Science* **231,** 1269 (1986).
9. Alexander, B. M., and Prieve, D. C., *Langmuir* **3,** 788 (1987).
10. Goldman, A. J., Cox, R. G., and Brenner, H., *Chem. Eng. Sci.* **22,** 653 (1967).
11. Prieve, D., C., Lanni, F., and Luo, F., *Faraday Discuss. Chem. Soc.* **83,** 297 (1987).
12. Bike, S. G., and Prieve, D. C., *Int. J. Multiphase Flow* **16,** 727 (1990).
13. Prieve, D. C., Bike, S. G., and Frej, N. A., *Faraday Discuss. Chem. Soc.* **90,** 209 (1990).
14. Prieve, D. C., and Frej, N. A., *Langmuir* **6,** 396 (1990).
15. Brown, M. A., Smith, A. L., and Staples, E. J., *Langmuir* **5,** 1319 (1989).
16. Brown, M. A., and Staples, E. J., *Langmuir* **6,** 1260 (1990).
17. Walz, J., and Prieve, D. C., *Appl. Opt.* **32,** 1629 (1993).
18. Ducker, W. A., Senden, T. J., and Pashley, R. M., *Langmuir* **8,** 1831 (1992).
19. Flicker, S. G., and Bike, S. G., *Langmuir* **9,** 257 (1993).
20. Lipson, S. G., and Lipson, H., "Optical Physics," 2nd ed. Cambridge Univ. Press, New York, 1981.
21. Axelrod, D., Burghardt, T. P., and Thompson, N. L., *Annu. Rev. Biophys. Bioeng.* **13,** 247 (1984).
22. Chew, H., Wang, D. S., and Kerker, M., *Appl. Opt.* **18,** 2679 (1979).
23. Verwey, E. J., and Overbeek, J. Th., "Theory of Stability of Lyophobic Colloids." Elsevier, Amsterdam, 1948.
24. van de Ven, T. G., Dabros, T., and Czarnecki, J., *J. Colloid Interface Sci.* **93,** 580 (1983).
25. Scales, P. J., Grieser, F., Healy, T. W., White, L. R., and Chan, D. Y. C., *Langmuir* **8,** 965 (1992).